Pareto Optimal Spectrally Selective Emitters for Thermophotovoltaics via Weak Absorber Critical Coupling

Nari Jeon[1], Jonathan J. Hernandez[2,4], Daniel Rosenmann[3], Stephen K. Gray[3], Alex B. F. Martinson[1],*, Jonathan J. Foley IV[4],*,

[1]Materials Science Division, Argonne National Laboratory, Argonne, Illinois, 60439, USA

[2]Union County College, 1033 Springfield Avenue, Cranford, New Jersey, 07016, USA

[3]Center for Nanoscale Materials, Argonne National Laboratory, Argonne, Illinois, 60439, USA

[4]Department of Chemistry, William Paterson University, 300 Pompton Road, Wayne, New Jersey, 07470, USA
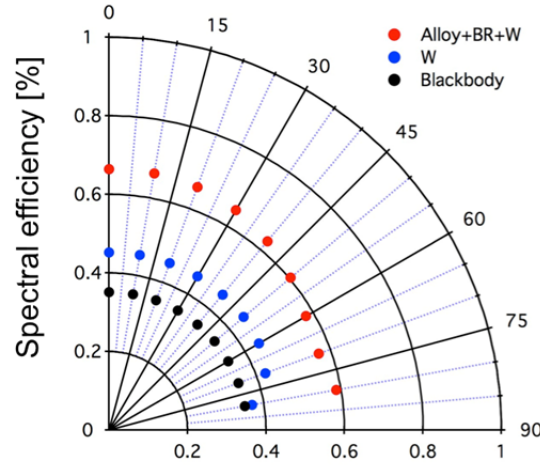
Angle Dependence of Spectral Efficiency

Figure S1. Spectral efficiency (%) of ideal alloy + BR + W, bare W substrate and blackbody at 1700 K calculated as a function of exit angle from 0 to 90°

Angle-dependence of Thermal Emission

A perfect blackbody is taken to have a cosine angle dependence[1]:

$$B(\theta, \lambda, T) = B(\lambda, T) \cos(\theta) \quad \text{(S1)}$$

where

$$B(\lambda, T) = \frac{2hc^2}{\lambda^5} \frac{1}{\exp\left(\frac{hc}{\lambda kT}\right) - 1}. \quad \text{(S2)}$$

Additionally, one can assume an equal admixture of s- and p-polarized emission at all angles. For real surfaces with emissivity that depends on polarization, angle, and wavelength, the thermally emitted power per unit wavelength per unit solid angle per unit area of the emitting surface can be given by

$$B(\theta, \lambda, T) \left(\frac{1}{2}\epsilon_P(\theta, \lambda) + \frac{1}{2}\epsilon_s(\theta, \lambda)\right) dA \, d\lambda \, d\Omega, \quad \text{(S3)}$$

such that the total useful power density averaged over the angles in the hemisphere enclosing the emitting surface is given by

$$P = \int_0^{2\pi} d\phi \int_0^{\frac{\pi}{2}} \sin(\theta) \, d\theta \int_0^{\lambda_{bg}} d\lambda \frac{\lambda}{\lambda_{bg}} B(\lambda, T) \cos(\theta) \left(\frac{1}{2}\epsilon_P(\theta, \lambda) + \frac{1}{2}\epsilon_s(\theta, \lambda)\right). \quad \text{(S4)}$$

38　For a perfect blackbody, $\epsilon_P(\theta,\lambda) = \epsilon_S(\theta,\lambda) = 1$ for all angles and wavelengths, so the
39　integration over all angles in the hemisphere contributes a factor of π to the spectral
40　density of a blackbody:

41
$$\rho(\lambda,T) = \int_0^{2\pi} d\phi \int_0^{\frac{\pi}{2}} \sin(\theta)\, d\theta\ \ B(\lambda,T)\cos(\theta) = \frac{2\pi hc^2}{\lambda^5}\frac{1}{\exp\left(\frac{hc}{\lambda kT}\right)-1}. \qquad (S5)$$

42　In calculating the useful power density for generating Fig. 2 in the main text, we make
43　the simplifying assumption that $\epsilon_P(\theta,\lambda) = \epsilon_S(\theta,\lambda) = \epsilon_{normal}(\lambda)$, where $\epsilon_{normal}(\lambda)$ is
44　computed from solving the Transfer Matrix Equations for the structure in question with
45　$\boldsymbol{\theta} = 0$; hence the use of $\rho(\lambda,T)$ in Equations (2), (3), and (4) in the main text.

46　We note that in Table 1, the Useful Power Density is reported only considering normal
47　emission angles because the angle dependence is not known for many structures reported
48　in the literature. The resulting normal Useful Power Density may be defined simply as

$$P_\perp = \int_0^{\lambda_{bg}} \frac{\lambda}{\lambda_{bg}} B(\lambda,T)\,\epsilon(\lambda)\,d\lambda. \qquad (S6)$$

49

50　A more realistic, albeit computationally expensive, approach requires solving explicitly
51　for $\epsilon_P(\theta,\lambda)$ and $\epsilon_S(\theta,\lambda)$ and numerically computing the integral in Equation (S5). We
52　use this approach to examine the angle dependence (**Figure S1**) of our selected structure
53　(see Figure 3 in the main text).

54

55

56

57

58

59

60

61

62

63

64   **Real and Imaginary Part of Refractive Index**

65
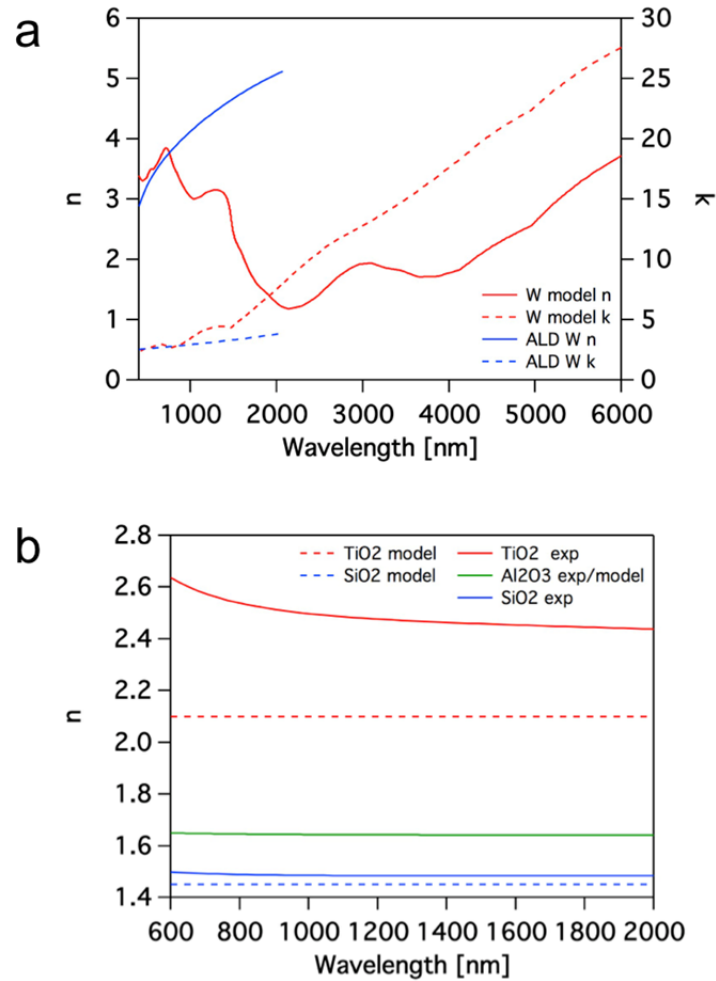
66

67

68   **Figure S2.** (a) Real (n) and imaginary (k) part of refractive index of tungsten. (b) Real
69   part of refractive index (n) of oxides. Solid lines are Cauchy-fit of measured **n** and dashed
70   lines are static values used for initial simulation (Figure 2).

71   The W refractive index data were adopted from Palik.[2] Ellipsometric spectra were
72   measured from fabricated oxides (Al_2O_3, TiO_2, SiO_2) and were fit by Cauchy models
73   with $n=A+B/x^2$ and $k=0$, where A and B are fitting parameters and x is wavelength. For
74   initial screening shown in Figure 2 and Figure 3, constant values of refractive indices are
75   used for TiO_2 (n=2.1, k=0) and SiO_2 (n=1.45, k=0), and Cauchy-fit of measured n values
76   was used for Al_2O_3.

77

78 **Effective Medium Approximations**

79   We employ two effective medium approximations for the tungsten-alumina alloys. The
80   first approximation is known as Maxwell-Garnett theory[3], within which the dielectric
81   function of the effective medium is given by

$$\epsilon_{alloy}^{MG} = \epsilon_D \frac{2f_W(\epsilon_W(\omega) - \epsilon_D) + \epsilon_W(\omega) + 2\epsilon_D}{2\epsilon_D + \epsilon_W(\omega) + f_W(\epsilon_D - \epsilon_W(\omega))}, \quad (S7)$$

82   where $\epsilon_W(\omega)$ denotes the dielectric function of tungsten, ϵ_D denotes the dielectric
83   function of the alumina dielectric material, and f_W denotes the volume fraction of
84   tungsten in the alumina surrounding medium. Bruggeman's effective medium
85   approximation is computed as[3]

$$\epsilon_{alloy}^{Br.} = \frac{b + \sqrt{8\epsilon_W(\omega)\epsilon_D + b^2}}{4} \quad (S8)$$

86   where

$$b = 2(1 - f_W)\epsilon_D + \left(2f_W - (1 - f_W)\epsilon_W(\omega)\right). \quad (S9)$$

87

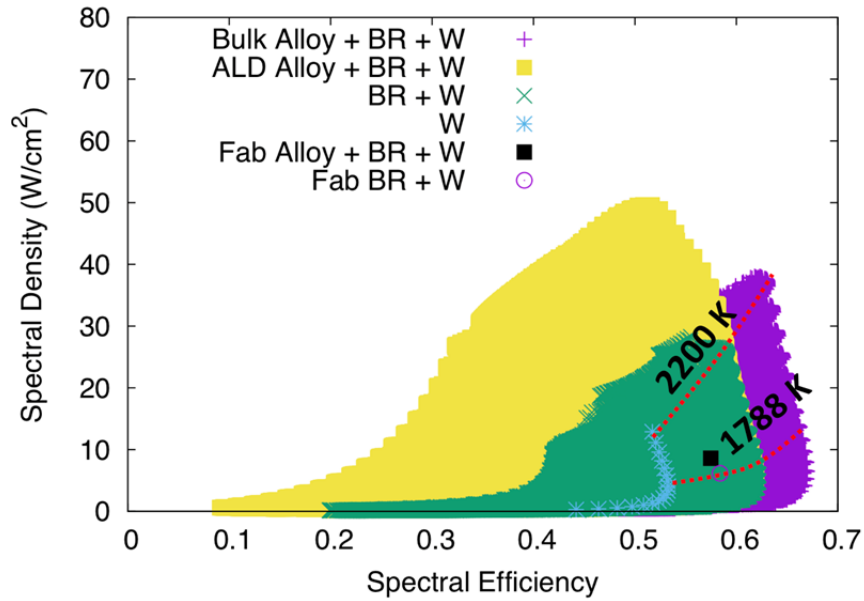88 **Pareto Optimal Solutions with Experimental Optical Constants**

89

90   **Figure S3.** Comparison of possible values for Spectral Density and Spectral Efficiency
91   for a variety of planar structures at temperatures between 1200K and 2200K when $\lambda_{BG} =$
92   2254nm. The class of planar structures include optically-thick tungsten (denoted 'W'),
93   variable Bragg reflectors with an optically-thick tungsten substrate (denoted 'BR + W'),

94 and variable W/Al$_2$O$_3$ alloys with variable Bragg reflectors with an optically-thick
95 tungsten substrate (denoted 'X Alloy + BR + W'), where X is either Bulk or ALD. We
96 utilize two models of the alloy: (1) where bulk W permittivity values are taken from Ref[2]
97 and Maxwell-Garnett effective medium approximation is used to model inclusions of W
98 in Alumina ('Bulk Alloy + BR + W', and (2) where ellipsometry data of ALD W is used
99 and the Bruggeman approximation is used to model inclusions of W in alumina 'ALD
100 Alloy + BR + W'). The permittivities for TiO$_2$ and SiO$_2$ are taken from ellipsometry of
101 ALD-deposited samples, as well

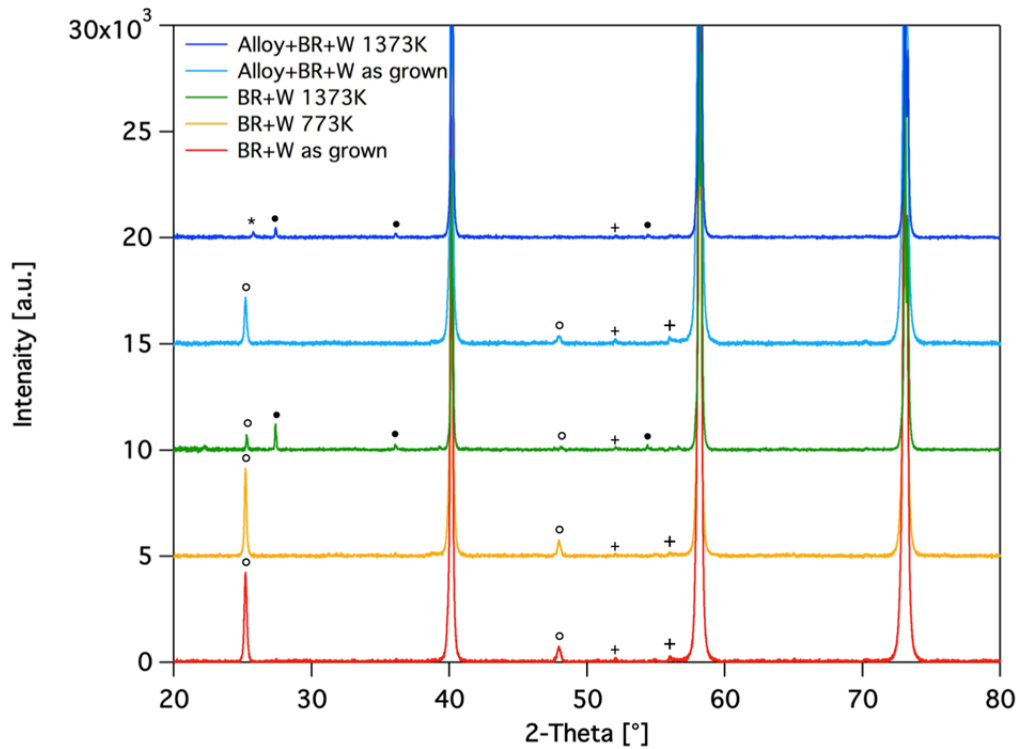102 **Bragg Reflector High Temperature Stability**

103

104 **Figure S4**. X-ray diffraction spectra of alloy + BR + W and BR + W before and after the
105 thermal emission measurements at 1373K. The three largest peaks at 40.1°, 58.1°, and
106 73.0° originate from W substrates.

107 As grown TiO$_2$ film exhibits anatase phase (°), which was stable upon annealing at 773K
108 for 2hr in air. The anatase phase partly transformed to rutile phase (•) upon annealing at
109 1373K for ~2 min in Ar for the thermal emission measurements. In contrast, no
110 crystalline peaks were detected for SiO$_2$ or Al$_2$O$_3$. Unassigned peaks marked as + are
111 intrinsic to the W substrate as they are observed in the bare W substrate as received. The
112 peak marked as * in the annealed alloy + BR + W is located at 0.6° higher angle than the
113 anatase TiO$_2$ peak (°) at 25.2°. The peak (*) may be WO$_{2-x}$ (JCPDF card #: 00-032-
114 1393), indicating possible oxidation of ALD W in the alloy layer at high temperature.
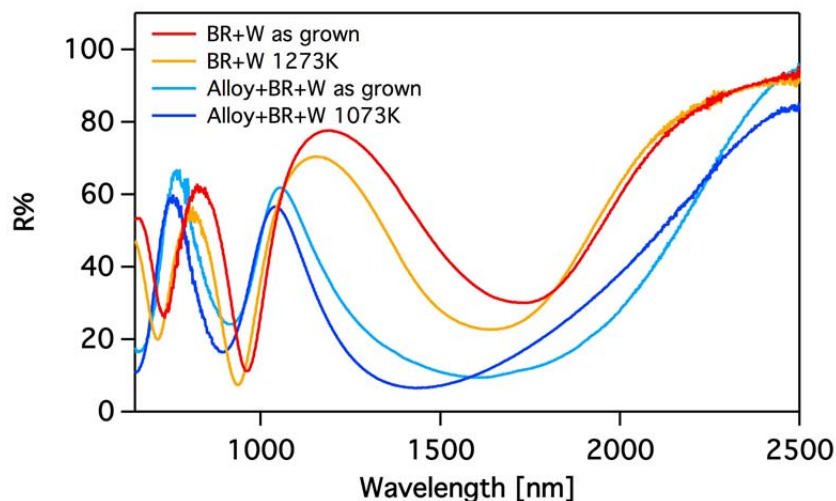
115

Figure S5. Reflectance spectra of alloy + BR + W and BR + W before and after annealing under Ar atmosphere at 1073K for 2hr and 1273K for 2hr, respectively.

As a result of annealing at 1273K for 2hr, fringes of BR + W structure were blue-shifted and the overall reflectance intensity decreased. The blue-shift of fringes maybe due to film densification. Similar to the BR + W sample, the fringes of alloy + BR + W sample were blue-shifted, and the reflectance intensity decreased. This suggests that the changes in reflectance of alloy + BR + W samples are mainly due to the changes in BR rather than the alloy layer.

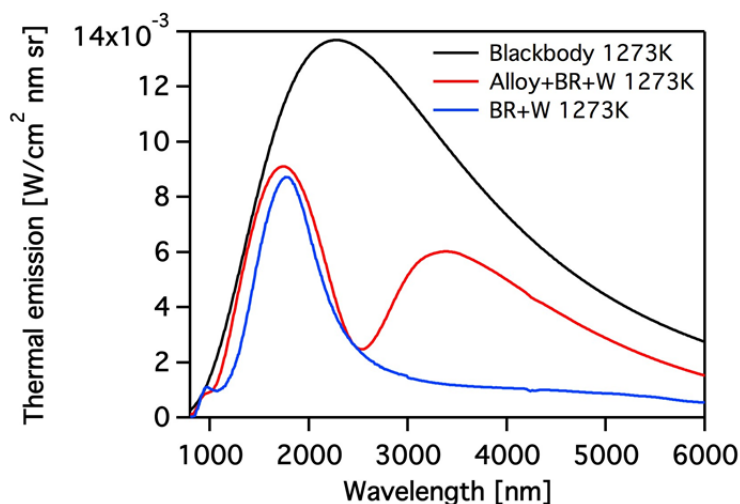**Comparison of alloy + BR + W and BR + W**

125

Figure S6. Measured thermal emission spectra of alloy + BR + W and BR + W at 1273K.

The emission of alloy + BR + W for wavelength < 2254 nm at 1273K is slightly enhanced compared to that of BR + W at the same temperature.

129

Transfer Matrix Equations

131 The Transfer Matrix Equations[4] for an L-layer structure with variations only along the z-
132 axis can be written as

$$\begin{pmatrix} E_1^+ \\ E_1^- \end{pmatrix} = \begin{pmatrix} M_{1,1} & M_{1,2} \\ M_{2,1} & M_{2,2} \end{pmatrix} \begin{pmatrix} E_L^+ \\ E_L^- \end{pmatrix}, \qquad (S10)$$

133 where the elements $M_{1,1}$ depend on the material properties (i.e. the refractive index n) and
134 the geometry of each layer, as well as on the frequency and polarization of incident light.
135 This formalism assumes that layer 1 and L are semi-infinte materials with real refractive
136 indices; however, all intermediate layers have finite thickness and may consist of
137 materials with complex refractive indices. The 2x2 **M** matrix can be computed from the
138 following product of matrices:

$$\begin{pmatrix} M_{1,1} & M_{1,2} \\ M_{2,1} & M_{2,2} \end{pmatrix} = \mathbf{D}_1^{-1} \left(\prod_{l=2}^{L-1} \mathbf{D}_l \, \mathbf{P}_l \, \mathbf{D}_l^{-1} \right) \mathbf{D}_L. \qquad (S11)$$

139 The **P** matrix is defined for each finite-thickness layer as

$$\mathbf{P}_l = \begin{pmatrix} \exp(i \, \phi_l) & 0 \\ 0 & \exp(-i \, \phi_l) \end{pmatrix}, \qquad (S12)$$

140 where $\phi_l = k_{z,l} \, d_l$ where d_l is the thickness of the lth layer of the structure,

$$k_{z,l} = \sqrt{\left(n_l \frac{\omega}{c} \right)^2 - \left(n_l \sin(\theta_1) \frac{\omega}{c} \right)^2}, \qquad (S13)$$

141 θ_1 is the angle of incidence of light at frequency ω upon the structure and n_l is the
142 refractive index of the lth layer at frequency ω. If the incident light is s-polarized, then
143 the **D** matrix for the lth layer has the form

$$\mathbf{D}_l = \begin{pmatrix} 1 & 1 \\ n_l \cos(\theta_l) & -n_l \cos(\theta_l) \end{pmatrix}, \qquad (S14)$$

144 while if the light is p-polarized, the **D** matrix for the lth layer has the form

$$\mathbf{D}_l = \begin{pmatrix} \cos(\theta_l) & \cos(\theta_l) \\ n_l & -n_l \end{pmatrix}, \qquad (S15)$$

145 where θ_l is the refraction angle in the lth layer determined by Snell's law.

146 The amplitudes E_1^+ and E_1^- are interpreted as the incoming and outgoing wave amplitudes
147 on the incident side, respectively; similarly, E_L^- and E_L^+ are interpreted is the incoming

148 and outgoing wave amplitudes on the terminal side, respectively. With access to the field
149 amplitudes and wavevectors, a number of useful quantities may be computed. For
150 example, the Fresnel reflection and transmission amplitudes may be computed as $r = \frac{E_1^-}{E_1^+}$
151 and $t = E_L^+$. For the analysis of reflection experiments, $E_1^+ = 1$ and $E_L^- = 0$ by
152 convention. Consideration of Eq. (S1) under these conditions leads to expressions for the
153 reflection and transmission amplitudes in terms of the elements of the **M** matrix,

$$r = \frac{M_{2,1}}{M_{1,1}} \qquad (S16)$$

$$t = \frac{1}{M_{1,1}}. \qquad (S17)$$

154 The reflection can then be calculated as $R = |r|^2$, the transmission as $T =$
155 $|t|^2 \frac{n_L \cos(\theta_L)}{n_1 \cos(\theta_1)}$. The absorption at a given frequency, which can be taken to be equal to the
156 emissivity by Kirchoff's law, can simply be computed as $\epsilon(\omega) = A(\omega) = 1 - T(\omega) -$
157 $R(\omega)$. The transfer matrix equations can be used to compute the stored energy of the
158 Bragg Relector ($P_{BR}(\omega)$) as well, which is a key quantity for assessing the degree of
159 critical coupling. Following the discussion by Piper and Fan[5], the amplitude associated
160 with the stored energy in a lossless resonant reflector (E_S) can be related to the incoming
161 and outgoing wave amplitudes according to

$$E_S = \left| \frac{E_1^- + E_1^+}{\sqrt{2\gamma_l}} \right|^2 \qquad (S18)$$

162 where γ_l is the leakage rate associated with the Bragg reflector. From Eq. S10, the stored
163 energy spectrum can be calculated for a given frequency as

$$E_s = \frac{(r+1)(r^*+1)}{2\gamma_l}. \qquad (S19)$$

164

165

166

167

168

169

170

171

Transmittance of SiC reference substrate
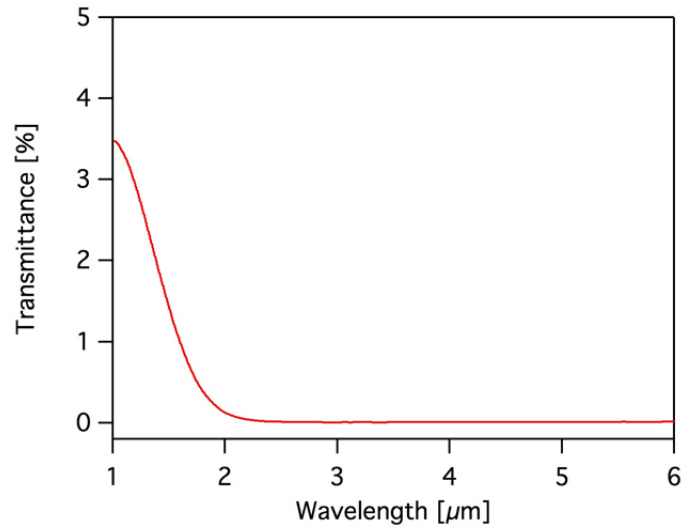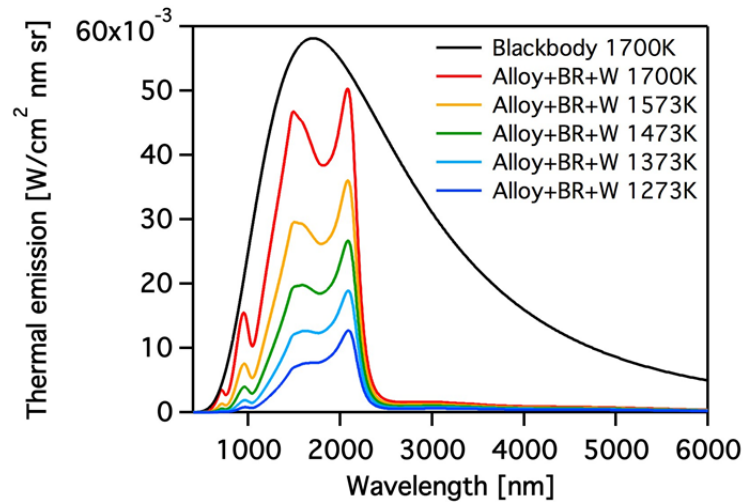

Figure S7. Transmittance of SiC substrate.

As the transmittance of SiC substrate was negligible over the examined wavelength range, we neglected the contribution of thermal emission of a heating cup underneath the sample to the measurement of thermal emission of the sample.

Sensitivity analysis for experimental variables

    1. Temperature

Figure S8. Calculated thermal emission spectra of designed alloy + BR + W structure at varied temperatures.

T [K]	1273	1373	1473	1573	1700
P [W/cm^2]	2.0	3.3	4.9	7.1	10.7
η_s [%]	64.4	65.7	66.3	66.6	66.4

Table S3. Spectral density (P) and spectral efficiency (η_s) of alloy + BR + W at varied temperatures

As an operation temperature decreases from 1700K to 1273K, the η_s decrease marginally while the P dramatically decreases.
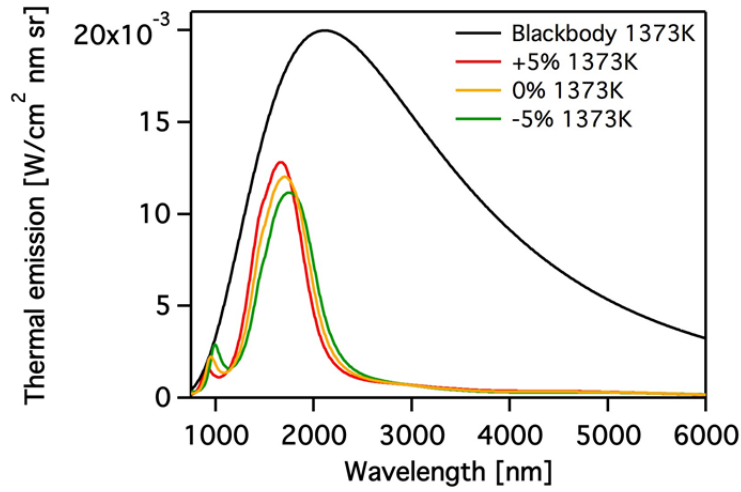
2. Oxide layer thickness

Figure S9. Thermal emission spectra of BR + W at 1373K for varied layer thickness. Red: 5% increased thickness from optimized structure; green: optimized structure; and blue: 5% decreased thickness from optimized structure.

Sample	Ideal Thickness	Ideal Thickness +5%	Ideal Thickness -5%
P [W/cm^2]	1.90	1.88	1.91
η_s [%]	60.2	60.6	59.3

Table S4. Spectral density P and spectral efficiency η_s of BR + W structures shown in Figure S9.

±5% change of thickness of oxides layer does not significantly alter both P and η_s.
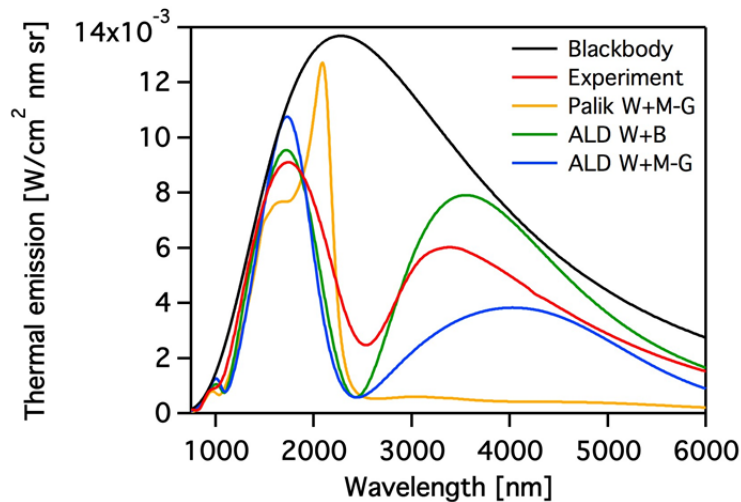
201 **3. Alloy model**

202

203 **Figure S10.** Thermal emission spectra of Alloy + BR + W at 1273K calculated from
204 varied alloy models and optical constants of W. Red: measured spectrum; yellow:
205 Maxwell-Garnett model with optical constants of Palik W, green: Bruggeman model with
206 optical constants of ALD W; blue: Maxwell-Garnett model with optical constants of
207 ALD W.

Sample	Measured	B + ALD W	M-G + ALD W	M-G + Palik W
P [W/cm^2]	1.9	1.7	1.7	2.0
η_s [%]	27.1	22.4	32.4	64.4

208 **Table S5**. Spectral density P and spectral efficiency η_s of alloy + BR + W

209 P and η_s may differ significantly depending on the model to describe refractive index of
210 alloy (Bruggeman vs. Maxwell-Garnett), and the refractive index of each constituting
211 element in alloy (Palik W vs. ALD W).

212

213

214

215

216

217

218

219

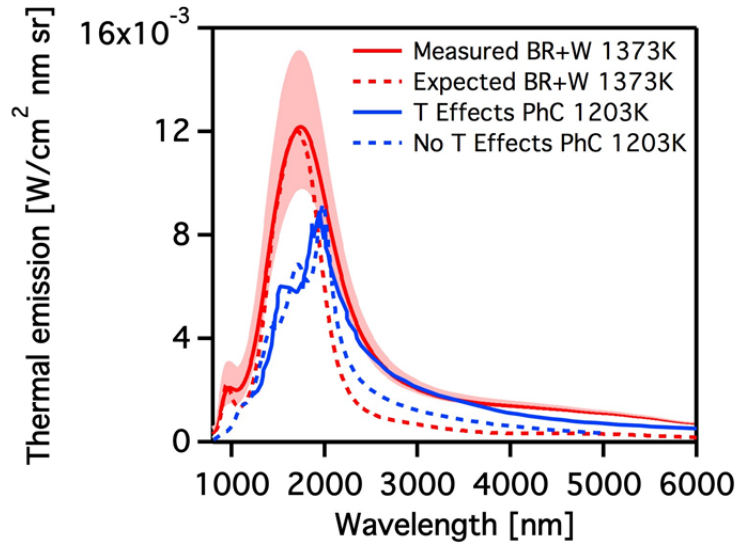220 **High Temperature Emission of Tungsten**

221

222 **Figure S11.** Comparison of thermal emission spectra of BR + W and W photonic crystal
223 (PhC) reported elsewhere.[6] A red solid line and red dashed line are the measured
224 spectrum and simulated spectrum of BR + W at 1373K. A blue solid line and blue dashed
225 line are the simulated spectra of W PhC (design II) at 1203 K with and without
226 considering the enhancement of thermal emission in infrared range at the temperature.

227 Yeng *et al.*[6] predicted the increase of thermal emission of W photonic crystal (PhC) in
228 the wavelength > 2,100 nm at high temperatures by fitting Lorentz-Drude parameters
229 from a measured emittance of flat W at high temperature.[6]

230 **Overall Thermophotovoltaic System Efficiency**

231 η_{TPV} as calculated here does not include other important factors in total
232 thermophotovoltaic system efficiency such as the PV cell (η_{PV}) and efficiency with
233 which the emitter structure can be heated (η_Q); the overall device efficiency will be a
234 product of these two efficiencies with the spectral efficiency (η_S).[7] The considerations
235 that are required to determine η_{PV} are complex and depend on factors including material
236 properties of the cell, the cell temperature, as well as the properties of the incident
237 radiation. An important contributing term to η_{PV} is the ratio of the open circuit voltage to
238 the band-gap voltage, $\frac{V_{op}}{V_{bg}}$, which increases asymptotically with increasing carrier density
239 generated in the cell.[8] This highlights the practical implications of the emitter figures of
240 merit: a high value of η_S will reduce thermalization losses in the cell, while a high value
241 of P minimizes loss of open-circuit voltage.

242 The thermophotovoltaic efficiency, η_{TPV}, of a hypothetical system may be predicted from
243 the parameters of relevant system previously reported. η_{TPV} is determined by the ratio of
244 electrical output power density from the solar cells (P_{el}) over radiant input power density
245 (P_{rad}).

$$\eta_{TPV} = \frac{P_{el}}{P_{rad}} \quad (S20)$$

246 This is based on the assumption that the view factor from emitter to cell is unity and
247 energy loss from the side surfaces of the emitter is negligible. The electrical output power
248 density is defined as

249 $$P_{el} = J_{SC}V_{OC}FF \quad (S21)$$

250 with J_{SC}, V_{OC} and FF, short-circuit current, open circuit voltage, and fill factor,
251 respectively.[9] J_{SC} is given by

$$J_{SC} = \int_0^{\lambda_g} \rho(\lambda,T)\,\epsilon(\lambda)\,SP(\lambda)\,d\lambda \quad (S22)$$

252 where $\rho(\lambda,T)$, $\epsilon(\lambda)$, and $SP(\lambda)$ are the blackbody spectral density, the emissivity
253 spectrum of the emitter, and the spectral response of the photovoltaic cell, respectively.[9]
254 Both J_{SC} and P are directly related with the thermal emission spectrum of the emitter.
255 Once J_{SC} was calculated from the measured thermal emission spectrum, $\rho(\lambda,T)\epsilon(\lambda)$, and
256 V_{OC} and FF values were retrieved for a given J_{SC} in the literature.[10] The radiant input
257 power density P_{rad} is defined as

$$P_{rad} = \int_0^{\infty} \rho(\lambda,T)\,\epsilon(\lambda)\,d\lambda \quad (S23)$$

258 η_{TPV} approaches η_S when one assumes an *ideal* PV cell with 100% FF and V_{OC} equal to
259 E_{bg} although this is not physically possible.[11]

260 **Reference**

261 1.   Lipson, A.; Lipson, S. G.; Lipson, H., *Optical Pyhysics* 4th edition ed.;
262 Cambdridge University Press: Cambridge, 2011.
263 2.   Lynch, D. W.; Hunter, W. R., Comments on the Optical Constants of Metals and
264 an Introduction to the Data for Several Metals A2 - Palik, Edward D. In *Handbook of*
265 *Optical Constants of Solids*, Academic Press: Burlington, 1997; pp 275-367.
266 3.   Bohren, C. F.; Clothiaux, E. E.; Huffman, D. R., *Absorption and Scattering of*
267 *Light by Small Particles*. Wiley-VCH: 2009.
268 4.   Yeh, P., *Optical Waves in Layered Media*. Wiley: 2005.
269 5.   Piper, J. R.; Fan, S., Total Absorption in a Graphene Monolayer in the Optical
270 Regime by Critical Coupling with a Photonic Crystal Guided Resonance. *ACS Photonics*
271 **2014,** *1* (4), 347-353.
272 6.   Yeng, Y. X.; Ghebrebrhan, M.; Bermel, P.; Chan, W. R.; Joannopoulos, J. D.;
273 Soljačić, M.; Celanovic, I., Enabling high-temperature nanophotonics for energy
274 applications. *Proceedings of the National Academy of Sciences* **2012,** *109* (7), 2280-2285.
275 7.   Zhou, Z.; Sakr, E.; Sun, Y.; Bermel, P., Solar thermophotovoltaics: reshaping the
276 solar spectrum. In *Nanophotonics*, 2016; Vol. 5, p 1.

277   8.   Rephaeli, E.; Fan, S., Absorber and emitter for solar thermo-photovoltaic systems
278   to achieve efficiency exceeding the Shockley-Queisser limit. *Opt. Express* **2009,** *17* (17),
279   15145-15159.
280   9.   Qiu, K.; Hayden, A. C. S.; Mauk, M. G.; Sulima, O. V., Generation of electricity
281   using InGaAsSb and GaSb TPV cells in combustion-driven radiant sources. *Solar Energy*
282   *Materials and Solar Cells* **2006,** *90* (1), 68-81.
283   10.   Chan, W.; Huang, R.; Wang, C.; Kassakian, J.; Joannopoulos, J.; Celanovic, I.,
284   Modeling low-bandgap thermophotovoltaic diodes for high-efficiency portable power
285   generators. *Solar Energy Materials and Solar Cells* **2010,** *94* (3), 509-514.
286   11.   Green, M. A., Solar cell fill factors: General graph and empirical expressions.
287   *Solid-state electronics 24* (8), 788-789.

288